

Title: Mitigation of Boundary Sampling Artifacts in Phase Space Generation for Electron FLASH Radiotherapy

Rafael Carballeira¹, Rongxiao Zhang^{1,3}, Kevin J. Willy¹, Hayley Cash⁴, David J. Gladstone^{1,2}

Thayer School of Engineering, Dartmouth College, Hanover, New Hampshire¹

Dartmouth Cancer Center, Lebanon, New Hampshire²

School of Medicine, University of Missouri, Columbia, Missouri³

Medical University of South Carolina, Charleston, South Carolina⁴

Abstract

Background: Monte Carlo-based treatment planning is essential for electron FLASH radiotherapy. Applicator-specific phase space (PHSP) files, recorded at the aperture exit reduce dose calculation time by 30–50% relative to traditional placement at the linac-exit window. Positioning PHSP scoring planes coincident with applicator-air interface introduces boundary sampling artifacts that have not been previously characterized in the electron PHSP literature.

Purpose: To identify and characterize a boundary sampling artifact arising in Geant4-based Monte Carlo simulations when PHSP scoring planes are positioned coincident with material-air interfaces, and to demonstrate its mitigation through systematic scoring plane offset for applicator-specific electron beam PHSP generation.

Methods: Applicator-specific PHSP files were generated using GAMOS 6.2.0 for a commissioned 9 MeV Mobetron UHDR Monte Carlo model across twelve clinical aperture configurations (2.5–10 cm diameter). Three scoring plane positions were evaluated relative to the physical aperture exit at 397 mm: coincident with the material-air interface (397 mm), 0.1 mm downstream (397.1 mm), and 1 mm downstream (398 mm). Dose calculations were benchmarked against linac-exit PHSP references and experimental water phantom measurements via distance-to-agreement (DTA) analysis.

Results: Scoring at the exact interface produced systematic proximal R50 shifts of up to 2.2 mm and DTA values of 4–6 mm for small-aperture configurations, exceeding the 3 mm clinical acceptance criterion. A 0.1 mm offset partially restored the primary electron energy spectrum but failed to recover the bremsstrahlung contamination tail. A 1 mm offset fully resolved all artifacts, achieving mean DTA values of 1.45 ± 0.63 mm (A6 series PDDs) and 2.00 ± 0.61 mm (A10 series PDDs), equivalent to or better than the linac-exit reference across all twelve configurations.

Conclusions: Boundary sampling artifacts in Geant4-based PHSP generation arise from the degenerate behavior of the fUseSafety step-limitation algorithm when safety = 0 at exact material boundaries, producing incomplete secondary electron equilibration and suppressed bremsstrahlung production in the scored particle population. A 1 mm downstream offset fully mitigates these artifacts while introducing negligible perturbation to primary beam characteristics. This offset requirement applies to any Geant4-based framework (including TOPAS and GATE) scoring PHSP files at applicator or collimator exit surfaces.

1. Introduction

Monte Carlo (MC) simulation is essential for accurate dose calculation in electron FLASH radiotherapy (FLASH-RT), where ultra-high dose rates exceeding 40 Gy/s produce biological responses that depend critically on both total dose and instantaneous dose rate.¹⁻² Analytical dose calculation algorithms cannot

reliably model the complex scattering characteristics of ultra-high-dose-rate (UHDR) electron beams, making MC-based treatment planning systems the required standard for clinical implementation³, particularly for dedicated delivery systems such as the Mobetron mobile electron linear accelerator.

A central component of any MC-based treatment planning workflow is the phase space (PHSP) file — a stored record of particle position, direction, energy, and type at a defined scoring plane — which allows the computationally expensive accelerator head transport to be performed once and reused across many dose calculations. In conventional workflows, PHSP files are recorded at the linac exit window and replayed for each plan, but this approach still requires full particle transport through 20–40 cm of applicator geometry per calculation which typically requires 45–60 minutes for the Mobetron system. Applicator-specific PHSP files recorded immediately downstream of the field-defining aperture eliminate this redundant transport entirely, reducing calculation time by 30–50% while establishing a direct correspondence between the clinical aperture selection and the computational source model.

Implementing applicator-exit PHSP files introduces a critical and previously undescribed technical challenge: the proximity of the scoring plane to a material-air interface. In Geant4-based frameworks including GAMOS, electron transport is governed by condensed history (CH) algorithms in which the G4UrbanMscModel approximates the cumulative effect of thousands of elastic scattering events into discrete transport steps.^{4,5,6} These multiple scattering (MSC) theories are mathematically valid only within infinite homogeneous media — an assumption that is necessarily violated when a step is truncated at a material boundary. At the exact interface, Geant4's internal safety parameter defined as the isotropic distance to the nearest boundary, used by the fUseSafety step-limitation algorithm to constrain step length evaluates to zero, removing the boundary-proximity constraint from the step calculation entirely. Under this degenerate condition, low-energy secondary electrons scattered from the aperture walls are recorded before their transport has equilibrated in air, bremsstrahlung production in foreshortened boundary-crossing steps is systematically suppressed, and lateral displacement corrections are underestimated. The net result is a corrupted phase space distribution that produces systematic errors in downstream dose calculations.

In initial attempts to implement applicator-exit PHSP files for the Mobetron UHDR system, these artifacts manifested as premature falloff in the percent depth dose (PDD) buildup region and proximal R50 shifts of up to 2.2 mm, with DTA errors reaching 4–6 mm for small-aperture configurations resulting in errors large enough to render the model clinically invalid under standard 3 mm acceptance criteria.³

This work presents a systematic investigation of these boundary sampling artifacts and their mitigation. We demonstrate that displacing the PHSP scoring plane 1 mm downstream of the physical aperture exit is both necessary and sufficient to resolve all artifacts across the full clinical range of Mobetron UHDR aperture configurations. The physical basis of this requirement in Geant4's condensed history transport step behavior, its sensitivity analysis, and its validation against experimental measurements are the primary contributions of this paper. The resulting applicator-specific PHSP library spans twelve clinical configurations (2.5–10 cm diameter, A6 and A10 series) and is suitable for immediate clinical implementation in MC-based FLASH-RT treatment planning.

2. Methods

2.1 Mobetron System and Applicator Configurations

All simulations were based on the Mobetron (IntraOp Medical Corp.), a dedicated mobile electron linear accelerator designed for UHDR radiotherapy. Field shaping is accomplished through interchangeable applicator cones and circular aperture inserts that define the treatment field at the patient surface.

Applicator configurations follow a naming convention encoding both cone geometry and field size. The prefix A6 or A10 denotes the applicator cone series — a 19 cm short cone and 28 cm long cone, respectively (Figure 1). The suffix I followed by a numerical value identifies the circular aperture insert diameter in centimeters. This study evaluated the full clinical range: seven A6 configurations spanning 2.5–6.0 cm diameter (Figure 2) and five A10 configurations spanning 6.0–10.0 cm diameter (Figure 3), for a total of twelve aperture configurations. This naming convention also establishes the direct aperture-to-PHSP correspondence central to the clinical workflow described here.

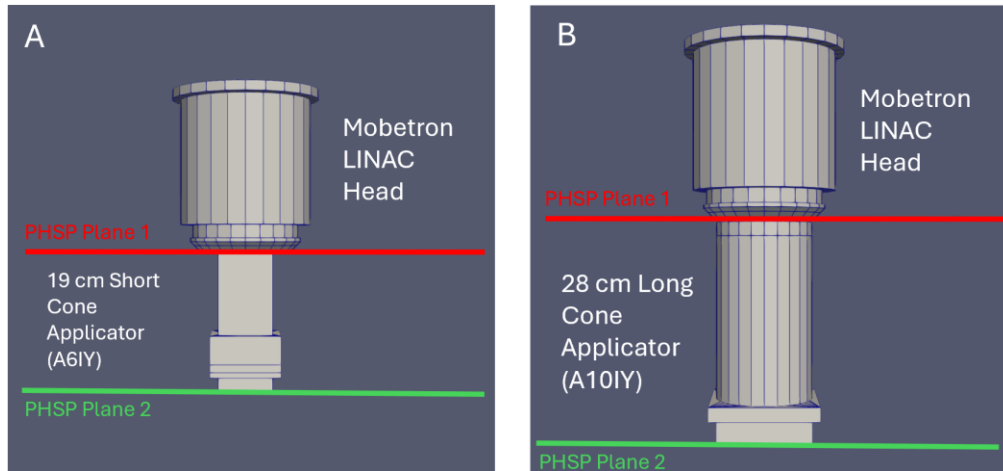


Figure 1A-B: Mobetron LINAC head visualizations for A) the 19 cm short cone applicator (A6IY) and B) the 28 cm long cone applicator (A10IY). Red lines indicate the Linac Exit PHSP plane (196 mm) and green lines indicate the Applicator Exit PHSP plane (398 mm).

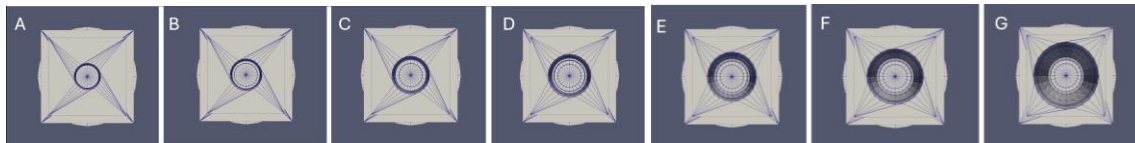


Figure 2A-G: A6IY configurations with aperture size, Y, following A) 2.5, B) 3, C) 3.5, D) 4, E) 4.5, F) 5, and G) 6 cm.

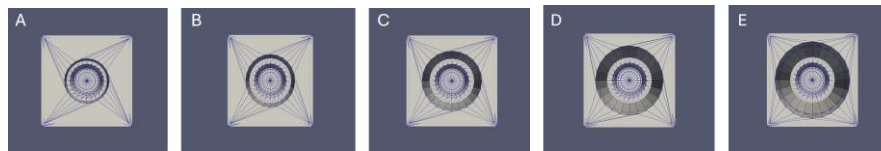


Figure 3A-E: A10IY configurations with aperture size, Y, following A) 6, B) 7, C) 8, D) 9, E) 10 cm.

2.2 Monte Carlo Simulation Framework

Simulations were performed using GAMOS version 6.2.0, a Geant4-based Monte Carlo platform for medical physics and radiation transport applications.⁶ The full Mobetron treatment head geometry was implemented via the GAMOS text geometry interface, explicitly modeling all beam-shaping components including the primary collimator, scattering foils, monitor chamber, secondary collimator, and applicator cone assembly for all twelve configurations following a previously published MC model.⁷ The aperture insert material in the simulation geometry is ACETAL (polyoxymethylene, density 1.41 g/cm³, composed of C₆H₁₄O₂), a low-Z acetal resin with $Z_{\text{eff}} \approx 5.7$.

Beam source parameters were derived from independent commissioning measurements: a Gaussian energy distribution (mean 9.58 MeV, sigma 0.173 MeV) and a Gaussian spatial distribution (sigma 1 mm) along the central axis. Particle transport was performed using the GmEMPhysics constructor, corresponding to Geant4's G4EmStandardPhysics (Option 0).^{4,5,6} This constructor employs the G4UrbanMscModel with the fUseSafety step-limitation algorithm, in which maximum step length is constrained by:

$$L = \max\{fR \times R_i, fS \times \text{safety}\} \quad 1$$

where $fR = 0.04$ is a range factor, R_i is the particle's remaining range, $fS = 0.6$ is a safety factor, and safety is the isotropic distance to the nearest geometry boundary.⁸ The skin parameter is 0, meaning single-scattering mode is never activated near boundaries. The behavior of this step algorithm at exact material boundaries — where safety = 0 — is central to understanding the artifacts investigated in this work and is discussed in detail in Section 4.1.

2.3 Phase Space File Generation and Boundary Offset Investigation

Applicator-specific PHSP files were generated using the GAMOS RTPPhaseSpaceUA user action, which records particle state at a defined axial Z position. All forward-directed particles were recorded without energy or angular filtering, capturing the complete population including primary electrons, secondary electrons, and bremsstrahlung photons. Particles were not terminated at the scoring plane (KillAfterLastZStop FALSE), ensuring downstream transport was unaffected by the recording. Files were stored in IAEA standard format with a maximum of 5×10^8 particles per file.

The central variable of this investigation was the axial position of the scoring plane relative to the physical aperture exit at 397 mm from the electron source — the surface at which the ACETAL aperture insert terminates and particles transition into air. Three positions were evaluated:

- 397 mm — coincident with the aperture material-air interface (baseline failure configuration)
- 397.1 mm — 0.1 mm downstream (sensitivity analysis)
- 398 mm — 1 mm downstream (corrected configuration)

Reference PHSP files were generated at the linac exit window position (196 mm from source) under identical simulation conditions. At this depth, the scoring plane intersects the open air bore along the central axis of the applicator assembly — surrounded by structural components at larger radii but not coincident with any material surface on-axis. Safety values are nonzero for all on-axis particles at this position, and the fUseSafety algorithm functions normally. This represents standard PHSP scoring practice and serves as the ground-truth benchmark for all comparisons.⁹

2.4 Dose Calculation and Experimental Validation

Dose calculation was performed in a 48 x 48 x 41cm water phantom with a 2 cm air gap between the applicator exit and the phantom entrance, utilizing a 1 mm voxel resolution for dose scoring. Experimental validation was conducted using an IBA Blue Phantom water scanning system equipped with a Flash Diamond field detector and IC-15 3573 reference detector for depth-dose measurements. Spatial accuracy between the simulated and measured data was quantified using distance-to-agreement (DTA) analysis, with a clinical acceptance criterion of <3 mm.³

3. Results

3.1 PHSP Plane Boundary Artifact Identification, Sensitivity, and Mitigation

Initial attempts to generate PHSP files with the scoring plane coincident with the physical aperture exit at 397 mm produced significant dosimetric discrepancies across all configurations tested. The A613 configuration is shown as a representative case in Figure 4. With the scoring plane at the exact material-air interface, the PDD exhibited a premature descent on the falloff slope and a proximal shift in R50 from the measured value of 3.42 cm to 3.20 cm — a 2.2 mm error (Figure 4A). DTA analysis across the full PDD curve yielded values of 4–6 mm for the smallest aperture configurations, well outside the 3 mm clinical acceptance criterion. Displacing the scoring plane 1 mm distal to the boundary at 398 mm fully restored the PDD, recovering R50 to 3.40 cm and matching measured data across the buildup, falloff, and bremsstrahlung tail regions (Figure 4A).

To characterize the minimum offset distance required for full transport stabilization, the scoring plane was evaluated at intermediate positions of 397.1 mm (0.1 mm offset) and 398 mm (1 mm offset), with the linac-exit reference scored at 196 mm for comparison (Figure 4B). The 0.1 mm offset produced partial recovery: R50 shifted from 3.20 cm to 3.30 cm and the steepness of the falloff slope improved, indicating that the primary electron energy spectrum began to stabilize. However, the bremsstrahlung contamination tail beyond approximately 5 cm depth remained significantly underrepresented relative to both the linac-exit reference and measured data. The 1 mm offset (398 mm) resolved both the falloff slope and the bremsstrahlung tail simultaneously with R50 = 3.40 cm vs measured 3.42 cm, achieving dosimetric equivalence to the linac-exit reference. This dissociation between R50 recovery and tail recovery establishes a two-stage recovery hierarchy: 0.1 mm is sufficient for primary electron angular equilibration after the final boundary-truncated step, but insufficient for the full secondary electron population to complete its range in air or for bremsstrahlung production events to occur in foreshortened steps.

To investigate whether alternative MSC configurations could mitigate the artifact without a geometric offset, simulations were repeated at the exact interface (397 mm) using the GmRadiotherapyPhysics physics list, which implements the fUseSafetyPlus step-limitation algorithm with Skin = 3 — activating explicit single scattering within three mean free paths of any geometric boundary (Figure 4C). This configuration produced partial recovery equivalent to the 0.1 mm geometric offset: R50 was restored from 3.20 cm to 3.30 cm and the buildup region was substantially improved, but the bremsstrahlung contamination tail beyond 5 cm remained underrepresented. The Skin = 3 result was indistinguishable from the 0.1 mm GmEMPhysics offset across the full depth range, indicating that single-scattering activation near the boundary recovers the same primary electron equilibration as a small geometric offset, but neither approach provides sufficient path length in air for radiative emission events to be sampled. Full recovery of both the R50 and bremsstrahlung tail required the 1 mm geometric offset regardless of MSC configuration. The physical mechanism underlying these observations is discussed in detail in Section 4.1.

To further characterize the phase space differences underlying the observed dosimetric recovery, angular distribution analysis was performed on the PHSP files generated for the representative A613 configuration at the 0 mm and 1 mm scoring plane positions. Energy spectra comparison between the two offsets revealed negligible differences across the full energy range, consistent with the artifact affecting a small secondary particle sub-population rather than the bulk energy distribution. The angular distribution, however, revealed a clear and physically interpretable signature of the boundary sampling artifact.

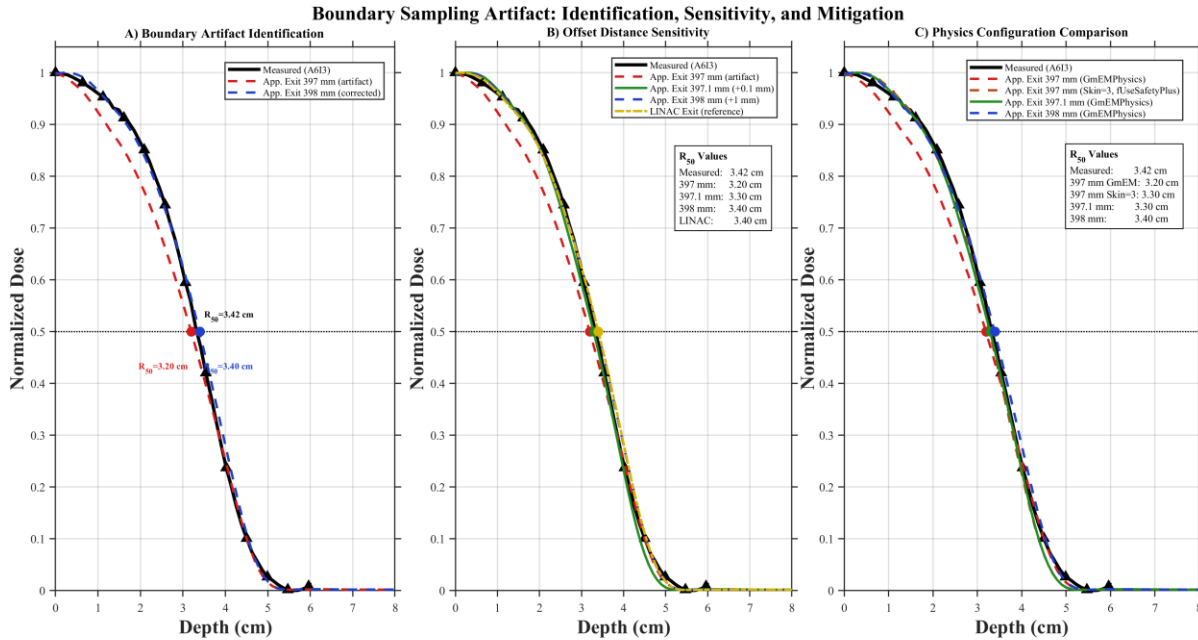


Figure 4: Boundary sampling artifact behavior for the representative A613 configuration. (A) Identification of the artifact: the PHSP scored at the exact material-air interface (397 mm, red) produces a 2.2 mm proximal R50 shift and premature PDD falloff relative to measured data (black), while a 1 mm downstream offset (398 mm, blue) restores agreement. (B) Offset distance sensitivity: 0.1 mm offset (green) partially recovers R50 but fails to restore the bremsstrahlung tail beyond 5 cm depth, while the 1 mm offset (blue) and linac-exit reference (gold) both achieve full recovery. (C) Physics configuration comparison: scoring at 397 mm with GmRadiotherapyPhysics (Skin = 3, fUseSafetyPlus, dark orange) produces recovery equivalent to the 0.1 mm GmEMPhysics offset (green) but cannot restore the bremsstrahlung tail; only the 1 mm geometric offset (blue) achieves full dosimetric equivalence with measured data.

3.2 Angular Phase Space Analysis

To further characterize the phase space differences underlying the observed dosimetric recovery, angular distribution analysis was performed on the PHSP files generated for the representative A613 configuration at the 0mm and 1mm scoring plane positions. Energy spectra comparison between the two offsets revealed negligible differences across the full energy range, consistent with the artifact affecting a small secondary particle sub-population rather than the bulk energy distribution. The angular distribution, however, revealed a clear and physically interpretable signature of the boundary sampling artifact.

To quantify the difference, the angular frequency difference between the 1mm and 0mm offset PHSP files was computed by binning all scored particles by angle with respect to the beam axis and subtracting the normalized 0mm distribution from the 1mm distribution; shown in Figure 6. At angles below approximately 5°, the 0mm offset PHSP contains an excess of particles relative to the 1mm offset (negative Δ Frequency), manifesting as a numerical pileup of near-forward particles artificially concentrated on-axis. This is the direct signature of the fUseSafety step-limitation failure: at the exact boundary where safety = 0, the proximity constraint on step length is removed entirely, allowing electrons to traverse the final boundary-crossing step without proper angular deflection and emerge

with artificially forward-directed trajectories. At angles between approximately 10° and 90°, the relationship inverts where the 1mm offset PHSP contains a consistent excess of particles (positive Δ Frequency), representing the large-angle secondary electron population that is physically present when transport equilibrates in air but absent from the 0mm PHSP due to boundary truncation. These are precisely the particles responsible for lateral dose buildup and the establishment of lateral scatter equilibrium at depth.

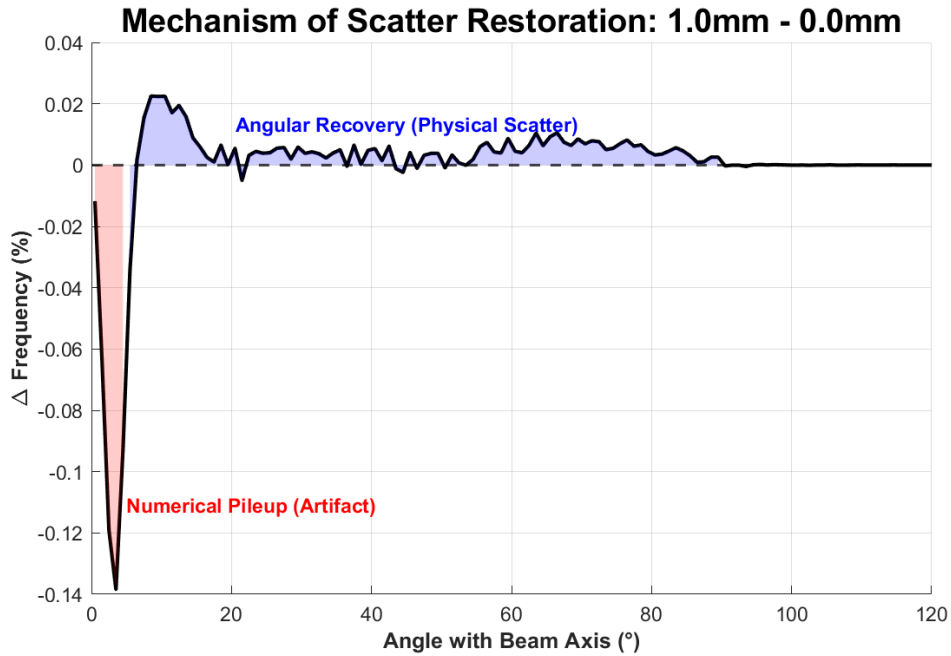


Figure 5: Angular frequency difference ($\Delta f(\theta) = f_{1\text{mm}}(\theta) - f_{0\text{mm}}(\theta)$) between the 1mm and 0mm offset applicator-exit PHSP files for the A6I3 configuration. The red shaded region (0–~8°) identifies the numerical pileup artifact — a near-forward particle excess in the 0mm PHSP. The blue shaded region (~10–90°) represents the recovered large-angle secondary electron population present in the 1mm offset PHSP but absent from the 0mm PHSP due to boundary truncation.

3.3 Global Validation Across All Aperture Configurations

Displacing the scoring plane by 1 mm distal to the physical boundary resolved these artifacts. As visualized in the blue dashed curve of Figure 4, the 1 mm air gap restored the R50 to 3.40 cm, achieving excellent agreement with experimental data. To demonstrate the robustness of this offset correction, we applied it across both the A6 (Figure 6A-B) and A10 (Figure 7) series. The corrected applicator-exit PHSP files (red curves) show consistent dosimetric equivalence to both the traditional linac-exit models (blue curves) and measured water-scan data (black curves) for both PDDs and lateral dose profiles.

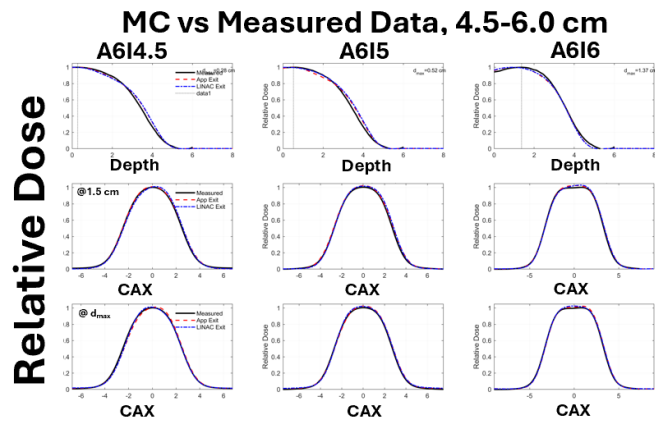
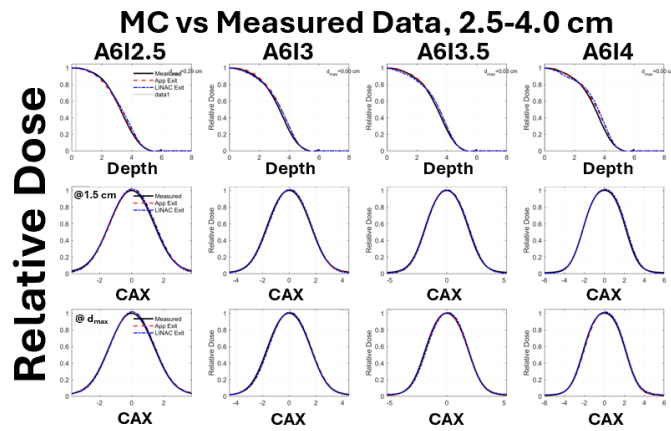


Figure 6A-B: A61X configuration PDDs and lateral profiles comparing applicator exit PHSP files (red), linac exit PHSP files (blue), and measured data (black).

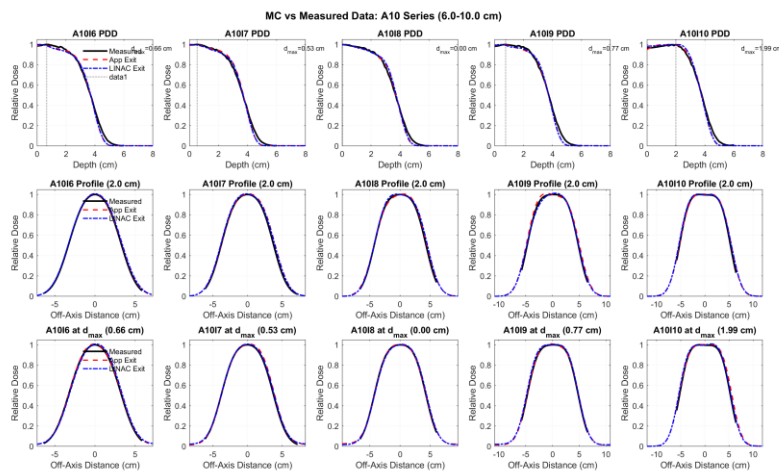


Figure 7: A10IX configuration PDDs and lateral profiles comparing applicator exit PHSP files (red), linac exit PHSP files (blue), and measured data (black).

3.4 Distance-to-Agreement Analysis

Quantitative spatial accuracy was assessed via DTA analysis across all twelve configurations and both PHSP generation methods (Figure 8). For the A6 series, applicator-exit PHSP files achieved mean PDD DTA values of 1.45 ± 0.63 mm (range: 0.60–2.29 mm) and mean lateral profile DTA values of 1.64 ± 1.34 mm (range: 0.50–3.66 mm). Linac-exit PHSP files performed comparably, with mean PDD DTA values of 1.55 ± 0.51 mm (range: 0.94–2.44 mm) and mean profile DTA values of 1.47 ± 1.36 mm (range: 0.50–3.66 mm). For the A10 series, applicator-exit PHSP files yielded mean PDD DTA values of 2.00 ± 0.61 mm (range: 1.21–2.64 mm) and mean profile DTA values of 1.75 ± 0.97 mm (range: 1.01–3.39 mm), while linac-exit files yielded mean PDD DTA values of 2.42 ± 0.86 mm (range: 1.38–3.21 mm) and mean profile DTA values of 2.01 ± 0.79 mm (range: 1.43–3.02 mm). All mean DTA values were well within the 3 mm clinical acceptance criterion.

Notably, applicator-exit PHSP files achieved equal or lower mean DTA values than linac-exit files for both the A6 and A10 PDD comparisons, confirming that eliminating redundant applicator transport does not degrade and in some configurations marginally improve spatial accuracy relative to the traditional approach. The DTA distributions in Figures 8C and 8D show narrow peaks centered near zero for both series, indicating that residual disagreement is predominantly at the 1 mm voxel resolution limit of the dose grid rather than reflecting systematic model error.

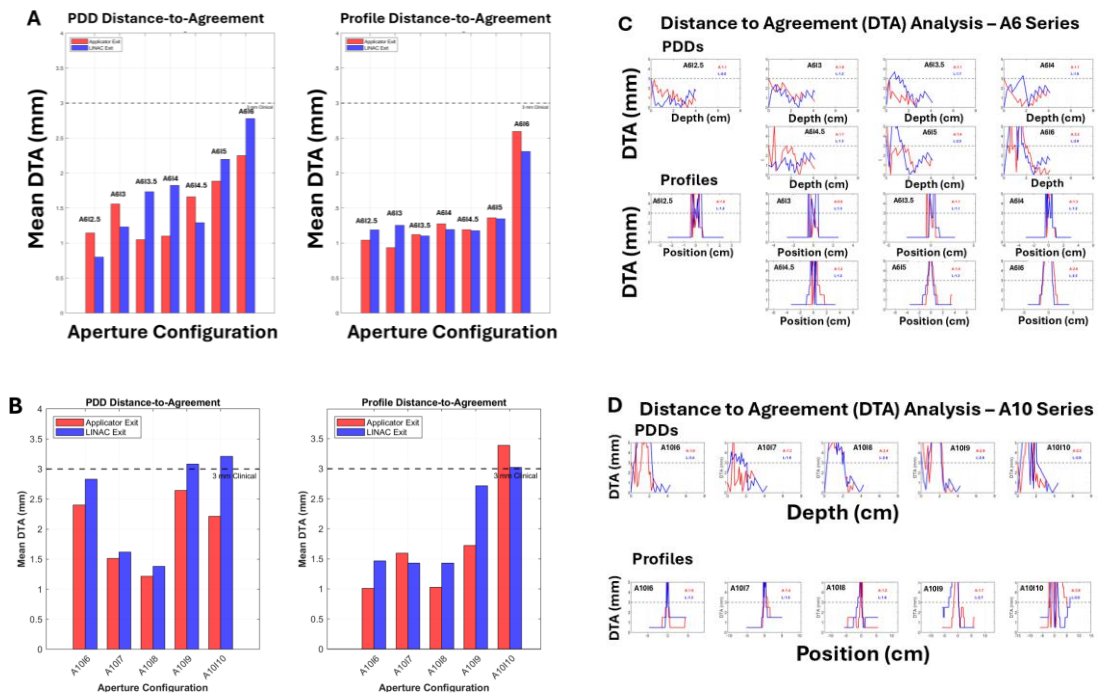


Figure 8A-D: Distance-to-agreement analysis for all aperture configurations. (A) A6 applicator series mean DTA values for PDDs (left) and lateral profiles at d_{max} (right). (B) A10 applicator series mean DTA values for PDDs (left) and lateral profiles at d_{max} (right). (C) DTA distributions for A6 aperture PDDs (left) and profiles (right). (D) DTA distributions for A10 aperture PDDs (left) and profiles (right). Red: applicator exit PHSP; blue: linac exit PHSP.

4. Discussion

4.1 Physical Mechanism of Boundary Sampling Artifacts

Geant4 simulates MeV-range electron transport using condensed history methods in which the G4UrbanMscModel approximates thousands of individual elastic scattering events into discrete transport steps governed by Lewis multiple scattering theory. This formalism assumes an infinite homogeneous medium over each step length — an assumption violated at material boundaries — and the consequences are well documented¹⁰: condensed history algorithms underestimate lateral displacement near interfaces and permit electrons to reach geometric boundaries in inappropriately large steps, producing dose errors of up to 39% in cavity geometries. The present work demonstrates that these same boundary-crossing artifacts corrupt PHSP files when the scoring plane is coincident with the interface.

The mechanism operates through three coupled failure modes. First, when a particle sits exactly on a material boundary, Geant4's safety parameter — the isotropic distance to the nearest geometry surface computed by G4Navigator — evaluates to zero. For the fUseSafety step limitation algorithm used by GmEMPhysics, the step limit is $L = \max\{fR \times R_initial, fS \times safety\}$. With $safety = 0$, the proximity constraint vanishes, and the algorithm defaults to $fR \times R_initial$ alone, which at 9 MeV in ACETAL may permit a first step in air of several millimeters without proper path-length correction. This degenerate condition is acknowledged in the Geant4 source code (G4CoupledTransportation): no safety update is performed when a particle is at a boundary.^{5,6}

Second, the final transport step within the aperture material is always truncated at the interface. The MSC model must re-estimate angular deflection and lateral displacement for a step shorter than the sampled physics mean free path. In Lewis multiple scattering theory, lateral displacement scales as s^2 — a particle accumulating small angular deflections over a longer path drifts laterally far more than one traveling a proportionally shorter distance — so truncating a step at the boundary systematically underestimates the lateral spread that would have accumulated over the full intended step length. Low-energy secondary electrons generated at the aperture wall undergo additional scattering before exiting the material; when the step is truncated at the exact boundary, these secondaries are clipped from the transport history before their trajectories stabilize in air. They are therefore absent from or incorrectly represented in the scored PHSP, producing a deficit of low-energy, large-angle particles responsible for buildup dose deposition. The proximal R50 shift and premature PDD falloff are the direct dosimetric signatures of this secondary electron deficit. This angular redistribution is directly visualized in Figure 5, which shows the near-forward particle excess in the 0mm PHSP (0–8°) and the corresponding deficit of large-angle secondaries (10–90°) that are recovered with the 1mm offset.

Third, bremsstrahlung photon production is suppressed in foreshortened steps. Energy that would otherwise be partitioned into discrete bremsstrahlung events is instead deposited via the continuous-slowing-down approximation, and secondary photons are never created. This suppression is distinct from the electron deficit above and operates on a different length scale, as confirmed by the comparison in Figure 4C: activating fUseSafetyPlus with $Skin = 3$ — which forces explicit single scattering within three mean free paths of any boundary — produced recovery equivalent to the 0.1 mm geometric offset, restoring R50 to 3.30 cm but leaving the bremsstrahlung tail underrepresented. Both small geometric offsets and improved boundary step handling can recover primary electron angular equilibration, but neither provides the path length in air required for secondary photon production events to be sampled. Only the 1 mm geometric offset resolves both components simultaneously.

An important geometric distinction explains why this artifact is specific to the applicator-exit scoring position and does not affect conventional linac-exit phase space scoring, despite the latter also crossing material structures. The relevant condition is not whether the scoring plane intersects any material interface, but whether the plane coincides with a material termination surface for particles on the

central axis. At 196 mm, the linac-exit plane intersects the open air bore along the central axis of the applicator assembly — no material surface is coincident with the plane on-axis, safety is nonzero for all central-axis particles, and `fUseSafety` functions normally even though window or scattering foil material exists at off-axis positions. At 397 mm, by contrast, the scoring plane coincides exactly with the physical termination surface of the ACETAL aperture insert across the entire scoring region including the central axis, where safety = 0 for every particle crossing it. The artifact therefore arises specifically when a scoring plane terminates a material structure on-axis with no further geometry downstream until the phantom — not from material-air interfaces in general. The aperture material is low-Z ACETAL rather than a high-Z metal, which makes this finding particularly noteworthy: the artifact is driven by the Geant4 transport step geometry at the boundary, not by the secondary particle yield of the material. This generalizes the concern to any on-axis material termination surface regardless of atomic number.

4.2 The 1 mm Recovery Distance

The sensitivity analysis establishes a clear two-stage recovery hierarchy. At 0 mm offset, the artifact is maximal: R50 is shifted 2.2 mm proximally and both the buildup region and bremsstrahlung tail are significantly distorted. At 0.1 mm offset, partial recovery occurs — R50 shifts to 3.30 cm, and the buildup discrepancy is reduced — but the bremsstrahlung tail persists. Full recovery requires the 1 mm offset, at which point both R50 and the bremsstrahlung tail match the linac-exit reference exactly.

This two-stage behavior reflects the distinct length scales required for two independent physical processes. The first stage — primary electron angular equilibration after the final boundary-truncated step — is recovered by either a 0.1 mm geometric offset or by activating explicit single scattering near the boundary via $S_{\text{kin}} = 3$, both of which restore R50 to within 0.1 cm of measured. The second stage — bremsstrahlung photon production and complete secondary electron transport in air — is recovered only by a full 1 mm offset. Low-energy secondaries (10–100 keV) produced at the aperture wall have ranges of roughly 0.1–1 mm in air;⁸ a 1 mm gap captures the full secondary electron population before recording. Bremsstrahlung production additionally requires electrons to complete a full physics step in air during which radiative emission can be sampled — at 9 MeV in air, a typical first step length is 0.5–1 mm, making 1 mm the threshold for photon production recovery as well.¹¹ The fact that improved MSC step handling alone cannot recover the bremsstrahlung tail confirms that the second stage is fundamentally a transport-distance problem rather than a step-calculation problem.

The 1 mm offset introduces negligible perturbation to the primary beam: energy loss across 1 mm of air at 9 MeV is under 0.01%, and angular spread changes are below 0.05°. The offset is therefore transparent to the primary beam while being sufficient to resolve all three failure modes.

4.3 Aperture Size Dependence

The severity of the boundary artifact scales inversely with aperture diameter. For the 2.5 cm A612.5 configuration, DTA errors reach 4–6 mm; for larger apertures the errors diminish. This reflects the geometric relationship between the open-field and wall-scattered particle populations. For small apertures, the perimeter-to-area ratio is high and a large fraction of the beam fluence consists of particles that have interacted with the collimator wall, which is the population most severely affected by all three failure modes. For large apertures, most particles traverse the open field without wall interaction, and boundary artifacts affect only a small fraction of total fluence. The practical implication is that boundary sampling artifacts are most dangerous precisely in the configurations where treatment fields are smallest and spatial precision is most critical.

4.4 Generalizability and Implementation Guidance

While demonstrated for a 9 MeV Mobetron system in GAMOS, the underlying mechanism is general to any Geant4-based simulation placing a PHSP scoring plane at a material-air interface. The condensed history boundary-crossing behavior described here is a property of Geant4's core tracking architecture, shared by TOPAS, GATE, and direct Geant4 applications.^{5,6} Users scoring phase space distributions at applicator or collimator exit planes in any of these frameworks should apply the same caution.

The practical recommendation depends on geometry constraints. When the simulation geometry permits, PHSP scoring planes should be positioned in air at least 1 mm downstream of any material surface, as this fully resolves both the primary electron equilibration and bremsstrahlung tail components of the artifact across all aperture sizes tested. A brief sensitivity analysis comparing R50 and the bremsstrahlung tail shape across at least three offset positions — at the interface, 0.1 mm, and 1 mm — is recommended for any new geometry before committing to a production PHSP library, with the smallest aperture configuration tested first as the most sensitive indicator of residual artifact. In situations where a 1 mm geometric offset is not feasible — for example, when the scoring plane must coincide with a specific physical surface for downstream simulation reasons — activating `fUseSafetyPlus` with `Skin = 3` (available in GAMOS via the `GmRadiotherapyPhysics` list, or in native Geant4 via `G4EmStandardPhysics_option4`)^{5,6} provides partial mitigation by recovering primary electron angular equilibration. This configuration restored R50 to within 0.1 cm of measured in the present work but did not eliminate the bremsstrahlung tail deficit, so users should weigh the residual photon contamination error against the geometric constraint when selecting between the two approaches.

A review of existing electron PHSP literature confirms that this boundary-offset requirement has not been previously characterized. The computational efficiency demonstrated here of 30–50% reductions in dose calculation time with equivalent dosimetric accuracy suggests that applicator-exit PHSP files represent a practical path toward the rapid MC-based treatment planning required for clinical FLASH-RT workflows, where the time constraints of UHDR delivery demand faster planning cycles than traditional linac-exit approaches can provide.

5. Conclusion

This work identifies and characterizes a previously undescribed boundary sampling artifact that arises in Geant4-based Monte Carlo simulations when PHSP scoring planes are positioned coincident with material-air interfaces and demonstrates its mitigation through a systematic offset strategy validated across twelve clinical Mobetron aperture configurations.

When the PHSP scoring plane was placed at the physical exit of the aperture insert (397 mm, coincident with the ACETAL material-air interface), systematic dosimetric errors were observed across all small-aperture configurations, with R50 shifts of up to 2.2 mm and DTA values reaching 4–6 mm. These artifacts arise from the degenerate behavior of Geant4's `fUseSafety` step-limitation algorithm at exact boundary positions: `safety = 0` removes the boundary-proximity constraint from step length calculation, secondary electron transport is clipped before equilibration in air, and bremsstrahlung production in foreshortened boundary-crossing steps is systematically suppressed. The low-Z nature of the aperture material confirms that the artifact is driven by the transport step geometry at the boundary rather than by secondary particle yield, generalizing the concern to any material interface.

Sensitivity analysis established that a 0.1 mm offset partially restores the primary electron energy spectrum but is insufficient to recover secondary photon contributions, while a 1 mm air gap fully resolves all artifacts — yielding dosimetric equivalence to linac-exit PHSP references and experimental measurements across all twelve configurations, with mean DTA values of 1.45 ± 0.63 mm (A6 PDDs) and 2.00 ± 0.61 mm (A10 PDDs), all within the 3 mm clinical acceptance criterion. This 1 mm boundary offset

introduces negligible perturbation to primary beam characteristics (energy loss < 0.01%, angular spread change < 0.05°) while being critical for PHSP data quality.

Beyond the Mobetron application, the boundary offset requirement described here applies to any Geant4-based simulation framework — including TOPAS and GATE — in which PHSP planes are scored at physical material surfaces. As applicator-exit phase space files become central to FLASH-RT and intraoperative electron radiotherapy, this finding represents an essential and previously uncharacterized implementation guideline for the MC simulation community.

Acknowledgments

The authors acknowledge NIH 1R21CA125760-01A1, NIH U01 CA260446-01A1, and the Norris Cotton Cancer Center Shared Resources with NCI cancer center support grant NIH 5P30 CA 23108-40. The authors graciously thank the guidance and advice provided by Dr. Jungwook Shin.

References

1. Vincent Favaudon et al., Ultrahigh dose-rate FLASH irradiation increases the differential response between normal and tumor tissue in mice. *Sci. Transl. Med.* 6,245ra93-245ra93(2014). DOI:10.1126/scitranslmed.3008973
2. Wilson JD, Hammond EM, Higgins GS and Petersson K (2020) Ultra-High Dose Rate (FLASH) Radiotherapy: Silver Bullet or Fool's Gold?. *Front. Oncol.* 9:1563. doi: 10.3389/fonc.2019.01563
3. Chetty, I.J., Curran, B., Cygler, J.E., DeMarco, J.J., Ezzell, G., Faddegon, B.A., Kawrakow, I., Keall, P.J., Liu, H., Ma, C.-M.C., Rogers, D.W.O., Seuntjens, J., Sheikh-Bagheri, D. and Siebers, J.V. (2007), Report of the AAPM Task Group No. 105: Issues associated with clinical implementation of Monte Carlo-based photon and electron external beam treatment planning. *Med. Phys.*, 34: 4818-4853. <https://doi.org/10.1118/1.2795842S>.
4. S. Agostinelli et al., Geant4—a simulation toolkit, *Nuclear Instruments and Methods in Physics Research Section A: Accelerators, Spectrometers, Detectors and Associated Equipment*, Volume 506, Issue 3, 2003, Pages 250-303, ISSN 0168-9002, [https://doi.org/10.1016/S0168-9002\(03\)01368-8](https://doi.org/10.1016/S0168-9002(03)01368-8).
5. P. Arce, J.I. Lagares, L. Harkness, D. Pérez-Astudillo, M. Cañadas, P. Rato, M. de Prado, Y. Abreu, G. de Lorenzo, M. Kolstein, A. Díaz, *Nucl. Instrum. Methods Phys. Res. A* 735 (2014) 304–313. <https://doi.org/10.1016/j.nima.2013.09.036>
6. Dai T, Sloop AM, Rahman MR, et al. First Monte Carlo beam model for ultra-high dose rate radiotherapy with a compact electron LINAC. *Med Phys.* 2024;51:5109–5118. <https://doi.org/10.1002/mp.17031>
7. Kawrakow, I. (2000), Accurate condensed history Monte Carlo simulation of electron transport. I. EGSnrc, the new EGS4 version. *Med. Phys.*, 27: 485-498. <https://doi.org/10.1118/1.598917>
8. R. Capote, et al., IAEA phase-space database for external beam radiotherapy, IAEA-TECDOC-1540, 2006. https://www-pub.iaea.org/MTCD/publications/PDF/te_1540_web.pdf
9. Poon, E. and Verhaegen, F. (2005), Accuracy of the photon and electron physics in GEANT4 for radiotherapy applications. *Med. Phys.*, 32: 1696-1711. <https://doi.org/10.1118/1.1895796>
10. Bielajew, Alex F., and D.W.O. Rogers. "Presta: The Parameter Reduced Electron-Step Transport Algorithm for Electron Monte Carlo Transport." *Nuclear Instruments and Methods in Physics Research Section B: Beam Interactions with Materials and Atoms*, vol. 18, no. 1-6, 1986, pp. 165–181, [https://doi.org/10.1016/s0168-583x\(86\)80027-1](https://doi.org/10.1016/s0168-583x(86)80027-1). Accessed 29 Jan. 2023.
11. Josep Sempau, et al. Monte Carlo Simulation of Electron Beams from an Accelerator Head Using PENELOPE. Vol. 46, no. 4, 1 Apr. 2001, pp. 1163–1186, <https://doi.org/10.1088/0031-9155/46/4/318>.

12. Rank L, Lysakovski P, Major G, et al. Development and verification of an electron Monte Carlo engine for applications in intraoperative radiation therapy. *Med Phys.* 2024;51:6348–6364. <https://doi.org/10.1002/mp.17180>
13. Almond, P.R., Biggs, P.J., Coursey, B.M., Hanson, W.F., Huq, M.S., Nath, R. and Rogers, D.W.O. (1999), AAPM's TG-51 protocol for clinical reference dosimetry of high-energy photon and electron beams. *Med. Phys.*, 26: 1847-1870. <https://doi.org/10.1118/1.598691>